

# Haptic bilateral teleoperation system for free-hand dental procedures

Lorenzo Pagliara, *Student Member, IEEE*, Vincenzo Petrone, *Member, IEEE*, Enrico Ferrentino, *Member, IEEE*, Andrea Chiacchio, Giovanni Russo, *Senior Member, IEEE*

**Abstract**—Free-hand dental procedures are typically repetitive, time-consuming and require high precision and manual dexterity. Robots can play a key role in improving procedural accuracy and safety, enhancing patient comfort, and reducing operator workload. However, robotic solutions for free-hand procedures remain limited or completely lacking. To address this gap, we develop a haptic bilateral teleoperation system (HBTS) for free-hand dental procedures (FH-HBTS). The system includes a mechanical end-effector, compatible with standard clinical tools, and equipped with an endoscopic camera for improved visibility of the intervention site. By ensuring motion and force correspondence between the operator's and the robot's actions, monitored through visual feedback, we enhance the operator's sensory awareness and motor accuracy. Furthermore, to ensure procedural safety, we limit interaction forces by scaling the motion references provided to the admittance controller based solely on measured contact forces. This ensures effective force limitation in all contact states without requiring prior knowledge of the environment. The proposed FH-HBTS is validated both through a technical evaluation and an in-vitro pre-clinical study conducted on a dental model under clinically representative conditions. The results show that the system improves the naturalness, safety, and accuracy of teleoperation, highlighting its potential to enhance free-hand dental procedures.

**Index Terms**—Haptics, teleoperation, interaction control, free-hand dental procedures, eye-hand coordination

## I. INTRODUCTION

THE World Health Organization estimates that oral diseases affect nearly 3.5 billion people worldwide. However, access to primary oral health services is limited due to the high costs of procedures, the unequal distribution of oral health professionals, and the lack of adequate healthcare facilities [1].

Traditionally, routine, prosthetic, periodontal, and some surgical dental procedures are performed free-hand. Routine procedures include the treatment of dental caries and endodontic therapy, while prosthetic procedures focus on the replacement of teeth through the use of prostheses. These procedures involve the preparation of the tooth, which entails the removal of hard tissue using rotary instruments mounted on dental handpieces [2]. Periodontal procedures include scaling and root planing (SRP), i.e., the removal of plaque and calculus from the teeth and the smoothing of root surfaces, typically

This research was conducted in the frame of the Department of Excellence 2023/2027 Project

Lorenzo Pagliara, Vincenzo Petrone, Enrico Ferrentino and Giovanni Russo are with the Department of Information Engineering, Electrical Engineering and Applied Mathematics (DIEM), University of Salerno, 84084 Fisciano, Italy, e-mail: {lpagliara, vipetrone, eferrentino, giovarusso}@unisa.it

Andrea Chiacchio is with the Specialization School in Oral Surgery, University of Naples Federico II, 80138 Napoli, Italy, e-mail: andr.chiacchio@studenti.unina.it

(Corresponding author: Lorenzo Pagliara)



Fig. 1: Manual (left) vs teleoperated (right) dental procedures (pictorial views).

employing hand instruments and inserts mounted on sonic or ultrasonic handpieces [3]. Finally, although robotic computer-assisted implant surgery (r-CAIS) have shown a significant increase in the accuracy of dental implant placement, many operators still prefer the free-hand method for dental implantology [4]. Each of these procedures requires accuracy, extensively trained manual skills, and dexterity.

**Remark 1.** *The oral cavity is a highly unstructured environment, which is full of natural obstacles that occlude the view of the surgical site and reduce the space for maneuvering, requiring constant changes in the orientation of the clinical tool and the operator's posture.*

Therefore, the successful outcome of a procedure, as well as the comfort for the patient, depend on both human factors, i.e., the experience and skills of the human operator [5], the adequacy of the instrumentation used and the duration of the treatments [6], and environmental factors [7], as highlighted in Remark 1. In particular, the latter factors can significantly affect the operator's comfort. In [8] a high prevalence of musculoskeletal disorders among dentists is reported. The main causes of these disorders can be traced back to an incorrect application of ergonomics, such as awkward postures, repetitive and prolonged movements, use of small or narrow tool handles, exertion of forces on hard or sharp objects, and exposure to vibrations [9]. Hence, when training new operators, much emphasis is placed on learning skills related to space utilization and positioning of surgical and non-surgical instruments, e.g., mirrors, to overcome occlusions, while maintaining healthy and comfortable postures [10]. In addition, to ensure the safety and effectiveness of the procedure, new

operators must acquire skills related to the correct amount of pressure to apply to the site of interest, depending on the type of tool used.

**Remark 2.** *The sense of touch plays a key role in achieving successful and efficient procedures.*

This is also apparent from emerging trends in teaching, which make use of virtual environments and haptic devices (HDs) for training new operators [11], [12].

In this context, the role of robots is to improve dental procedures, in terms of both patient satisfaction, i.e., broader access to care, reduced treatment time, and fast recovery, and operator comfort, i.e., reduced workload intensity, increased visibility of the surgical field, and improved ergonomics [13], as shown in Figure 1.

#### A. Related works

Haptic teleoperations are an enabling technology for the remote execution of complex tasks, employing a robotic system.

**Remark 3.** *Haptic teleoperations combine the robot skills with the flexibility, dexterity, and cognitive capabilities of humans, while overcoming barriers in terms of distance, hazardous environments, and scales beyond human reach.*

By providing multiple types of sensory information, i.e. visual and haptic feedback, HBTs enable the human operator to experience *telepresence* [14]. Furthermore, by integrating different haptic feedback and guidance modalities [15], [16], and shared control approaches [17], they contribute to reducing errors and enhance the efficiency, accuracy and safety of procedures, while also improving operator comfort and confidence. For these reasons, such technology is consolidated in, e.g., telesurgery, space exploration, and the handling of hazardous materials in nuclear or underwater environments. However, in the context of dentistry, its adoption is still very limited.

The majority of research in robotics for dentistry is focused on oral implantology [18], mainly because robotic implant surgery offers significant benefits in terms of implant accuracy in partially [19] or totally edentulous patients. Such technology also enables flapless implant placement, accelerating recovery time, reducing postoperative pain, and enhancing patient comfort [20]. [21] shows that a telerobotic-assisted drill can enhance accuracy while preserving awareness through an effective transmission of cutting forces and vibrations.

On the other hand, the state-of-the-art shows considerably less research effort in other free-hand procedures, a trend also highlighted in existing reviews of dental robotics [22], which report a strong imbalance in favor of implantology. Despite this imbalance, the literature reports evidence of the potential benefits of robotic technologies in free-hand dental procedures. Such evidence is analyzed in the following and summarized in the supplementary materials<sup>1</sup>. The analysis focuses on robotic systems explicitly developed for dental

procedures and directly interacting with the oral environment, aiming at supporting or automating clinical free-hand procedures, while excluding works specifically addressing oral implantology. Only approaches supported by experimental, in vitro, or preliminary validation are considered, whereas purely virtual studies or robotic solutions not specifically tailored to dental procedures are not included.

In the context of prosthetic procedures, robotics can enhance the precision of manual grinding using a turbine drill during tooth preparation [23] and can compensate for hand tremors and the lack of tactile feedback in laser ablation [24], [25]. This can improve accuracy [26] and efficiency [27], and can enable automated tooth arrangement [28] and preparation for veneers and full crowns [29], [30]. In endodontics, robotics can automate and enhance precision and efficiency in root canal treatments [31], [32], outperforming current approaches also in effectively addressing biological and mechanical traits associated with biofilm recalcitrance and reinfection [33], and can support visual-guided tool navigation [34]. In periodontal procedures, robots have the potential to increase accuracy, reducing the risk of errors and trauma to tissues by optimizing applied forces, as with other free-hand procedures. They can also improve the ergonomics for the operator, and comfort for the patient by reducing recovery time. However, for such procedures, robotic technologies are still lacking [35], and there is no empirical evidence of such advantages. Existing systems addressing force-regulated interaction with teeth are limited to adjacent tasks, such as tooth-brushing assistance [36], and are not designed for direct periodontal procedures.

Thus, although robotics shows promise in dental practice, several limitations remain. First, the quality of research is still insufficient in terms of clinical validation and technology readiness level (TRL) [37]. This is heavily influenced by the high costs of these systems and the need to ensure their compatibility with existing clinical tools [38]. Second, the most widespread robots are autonomous, which require the development of advanced capabilities in perception, recognition, and exception handling [38]. In this context, the presence of a human is still necessary not only as a supervisor but also as an operator. In light of Remark 2 and Remark 3, and considering the impact on the operator acceptance [39], haptic teleoperations represent a viable solution. Moreover, HBTs would allow the acquisition of human control strategies directly exercised in the robot state space, simplifying the process of transferring the knowledge from the human to the robot [40] and enabling the effective and objective evaluation of operator skills during training [41]. However, as emerges from the literature analysis above, no robotic solutions based on haptic bilateral teleoperation have been reported for free-hand tasks. Finally, research tends to prioritize oral implantology over other dental procedures, despite the high number of daily free-hand routine procedures and the less invasiveness, entailing better patient acceptance [42]. Considering these limitations, [22] recommends to shift the focus from oral implantology towards less invasive procedures, which are better suited as forerunners in the field, and also to invest in educational robotics research as a valuable tool to overcome the barrier of acceptance of robotic systems among future dentists.

<sup>1</sup>This paper has supplementary downloadable material available at <http://ieeexplore.ieee.org>, provided by the authors. This includes a supplementary PDF format information file and a multimedia MOV format movie clip, showing the end-to-end system experimental demonstration. This material is 78.5 MB in size.

## B. Contributions

Motivated by the limitations or complete absence of robotic solutions for the most repetitive free-hand dental procedures, and in light of the advantages introduced by haptic teleoperations, as in Remark 3, we propose a HBTS for free-hand dental procedures (FH-HBTS). The proposed system features a custom designed end-effector, compatible with existing clinical tools, and a dedicated haptic control system that ensures procedural safety, improves accuracy, and preserves manual dexterity. Therein, key contributions are: (1) an eye-hand coordination controller providing both motion and force correspondence between the HD's workspace and the video stream coming from the eye-in-hand camera; with respect to existing HBTSs, such mapping is bilateral and drift-free, even after prolonged teleoperation sessions; (2) a force limitation strategy effectively reducing interaction forces; with respect to existing HBTSs, this strategy needs no previous assumption or online estimation of the environment geometry, therefore accounting for the challenges outlined in Remark 1; notably, this strategy is part of the onboard robot controller and is therefore compatible with passivity-based teleoperations; (3) an integrated TRL-5 system for free-hand dental procedures, validated on SRP, demonstrating technical feasibility and clinical suitability.

In light of the inclusion and exclusion criteria defined in Section I-A, and also reported in the supplementary materials, to the best of the authors' knowledge, this is the first HBTS specifically complying with the special requirements of safety, accuracy, and dexterity characterizing free-hand dental procedures.

## II. PRELIMINARIES

### A. Notation

We denote by  $\mathbf{T}_b^a \in SE(3)$  the homogeneous transformation matrix from frame  $a$  to frame  $b$ , in the form:

$$\mathbf{T}_b^a = \begin{pmatrix} \mathbf{R}_b^a & \mathbf{p}_b^a \\ \mathbf{0}^\top & 1 \end{pmatrix}, \quad (1)$$

where  $\mathbf{R}_b^a \in SO(3)$  is the rotation matrix from frame  $a$  to frame  $b$ , with  $\mathbf{R}_a^b = (\mathbf{R}_b^a)^{-1} \equiv (\mathbf{R}_b^a)^\top$ , and  $\mathbf{p}_b^a \in \mathbb{R}^{3 \times 1}$  represents  $b$ 's origin in frame  $a$ .

We let  $\mathbf{x}_b^a = [(\mathbf{p}_b^a)^\top, (\mathbf{q}_b^a)^\top]^\top$  be the pose of the frame  $b$  with respect to the frame  $a$ , corresponding to  $\mathbf{T}_b^a$ , where  $\mathbf{q}_b^a \in \mathbb{H}_1$  is the quaternion associated with  $\mathbf{R}_b^a$ .

We denote by  $\mathbf{R}_a^{\mathcal{F}}(\alpha) \in SO(3)$  the elementary rotation of an angle  $\alpha$  about a generic axis  $\mathbf{a}$  of a frame  $\mathcal{F}$ .

We denote by  $\mathbf{v}_b^a = [(\dot{\mathbf{p}}_b^a)^\top, (\boldsymbol{\omega}_b^a)^\top]^\top \in \mathbb{R}^{6 \times 1}$  the twist of the frame  $b$  with respect to the frame  $a$ , where  $\dot{\mathbf{p}}_b^a, \boldsymbol{\omega}_b^a \in \mathbb{R}^{3 \times 1}$  are the linear and angular velocities, respectively.

We let  $\mathbf{h}^a = [(\mathbf{f}^a)^\top, (\mathbf{m}^a)^\top]^\top \in \mathbb{R}^{6 \times 1}$  be the wrench with respect to the frame  $a$ , where  $\mathbf{f}^a, \mathbf{m}^a \in \mathbb{R}^{3 \times 1}$  are the forces and momenta, respectively.

$\mathbf{I}_n$  indicates the  $n \times n$  identity matrix.

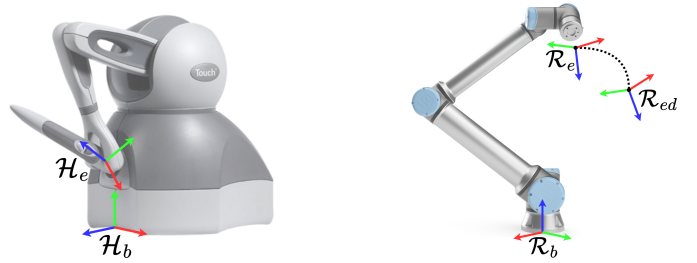


Fig. 2: Haptic device and robot reference frames.

### B. Haptic device and robot reference frames

The frames used by the HD and the robot are reported in Figure 2. With regard to the HD, two frames are introduced:  $\mathcal{H}_b$  is the base reference frame, in which the HD's stylus poses and the feedback forces are expressed;  $\mathcal{H}_e$  is the HD's stylus frame. Regarding the robot, four frames are defined:  $\mathcal{R}_b$  is the base reference frame, in which motion references are expressed;  $\mathcal{R}_e$  is the robot's end-effector frame (computed from forward kinematics of joint measurements), corresponding to the tool center point (TCP);  $\mathcal{R}_{ed}$  is the desired robot's end-effector frame, input to admittance control;  $\mathcal{R}_c$  is the compliant frame, output by the admittance control law.

We note that, after admittance control, motion control guarantees that  $\mathcal{R}_e$  tracks  $\mathcal{R}_c$ , as discussed next.

## III. METHODOLOGY

The FH-HBTS we propose, shown in Figure 3, is based on a position-position architecture [43], coupling the leader (LR) and follower (FR) robots by means of a spring-damper, which is a passive element. Therefore, in the absence of communication delays, this architecture has the advantage of being intrinsically stable [44], [45]. A formal proof of absolute stability can be found in [46]. In the proposed design, we assume negligible time delays and packet losses and, accordingly, do not integrate passivity-based control approaches [47]. This choice is motivated both by the validity of this assumption in healthcare facilities and by the conservative nature of passivity-based methods, which are known to worsen transparency and system usability in order to ensure stability under adverse network conditions [48]. Indeed, in precision free-hand dental procedures, this trade-off is generally undesirable, as it may impair fine force discrimination and the naturalness of the interaction. Nevertheless, the management of communication delays and packet losses represents an orthogonal direction to the one investigated in this work. Indeed, under non-ideal network conditions, the proposed architecture can be readily extended to enforce time-domain passivity of the communication channel, for instance by adopting a TDPA-based approach [49], as demonstrated in Section IV-B.

The LR is an impedance HD, sensing the pose of the operator and rendering haptic feedback according to the remote interaction between the FR and the environment. The HD is controlled by a leader controller, featuring an eye-hand coordination controller (EHCC) and a haptic feedback controller (HFC). The former is responsible for capturing the

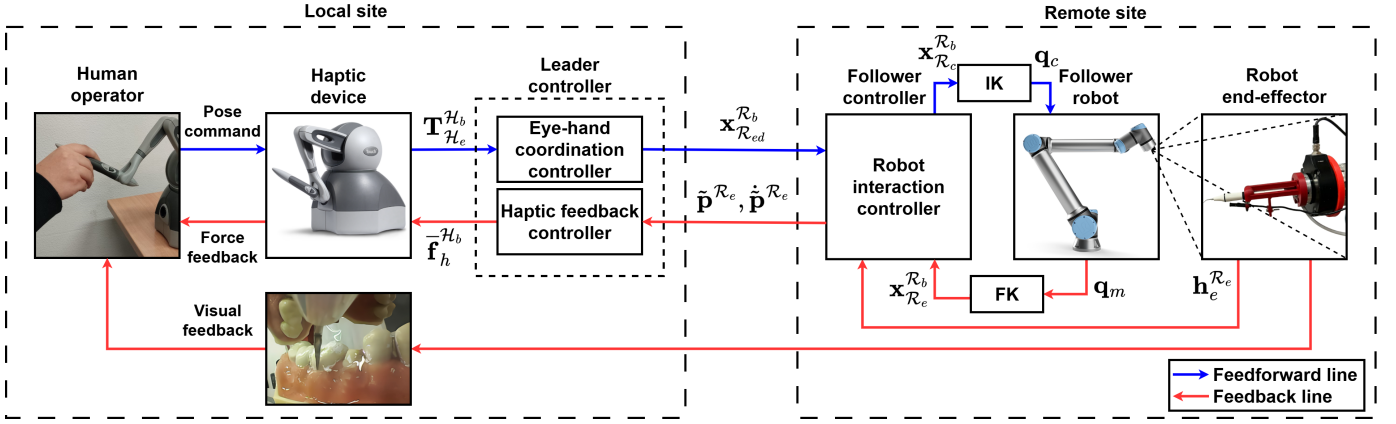


Fig. 3: Haptic bilateral teleoperation system scheme.

HD's stylus poses, filtering human tremors, and generating the corresponding robot end-effector poses, so that the robot follows the stylus motion in coordination with the visual feedback. The latter is responsible for rendering the force feedback on the HD to let the human operator perceive the remote environment. Both controllers record data throughout the entire procedure. The FR is a position-controlled robot, instructed to track the HD through an admittance controller, which provides a configurable degree of compliance on its target pose with respect to the environment and improves safety through dedicated mechanisms and emergency protocols.

With reference to Figure 3, depicting the complete system, the following sections examine its individual subcomponents in detail. Section III-A and Section III-C provide a detailed description of the objectives and operation of the EHCC and HFC controllers. Section III-B describes the robot interaction control. Finally, Section III-D presents the design of the mechanical end-effector for the FR.

#### A. Eye-hand coordination controller

In a HBTS, visual feedback plays a crucial role in overcoming the limitations caused by distance. In teleoperated free-hand dental procedures, using an eye-in-hand camera is the most effective solution [50]. This approach enables the operator to maintain a consistently centered view of the operative field, offering a significant advantage over eye-to-hand camera configurations, where the view may be off-center with respect to the area of interest or obstructed by physical obstacles. In this context, the human operator relies on the video of the camera to command the FR via the HD. However, in the eye-in-hand configuration, a rotation of the tool (unavoidable, to preserve dexterity) causes a rotation of the viewing angle, whose lack of compensation results in a loss of both motion and force correspondence between the movements and perceived interaction expected by the operator and those actually executed by the robot in the camera view. This highlights the importance of an appropriate coupling.

The literature shows that this coupling can be achieved through simple kinematic transformations and scaling strategies [51]. Common mapping strategies include position control, workspace drift control [52], and rate control [53] which

define how the operator's motions are translated into robot commands, complemented by force scaling [51] to map the interaction forces into the range of forces that the HD can exert. However, these methods generally neglect viewing angle effects, relying on display-level compensation and thus compromising force correspondence. Indeed, the da Vinci Surgical System<sup>TM</sup>, which requires the insertion of multiple tools to implement an eye-to-hand strategy, thereby increasing bulk and cost of the equipment, provides the motion correspondence by projecting the endoscope image above the surgeon's hands by means of mirrored overlay optics [54]. In a similar manner, in eye-in-hand cases, motion correspondence is typically achieved by aligning the visual feedback with the operator's control frame through online compensation of camera-control frame misalignment in the displayed view [55].

To overcome this limitation, we introduce an eye-hand coordination mapping preserving both motion and force correspondence. Within the proposed EHCC, this mapping is implemented through a view-consistent transfer of the HD twist to the FR and incorporates dynamic scaling factors to improve control accuracy according to task requirements. To enhance the naturalness of the teleoperation, a rotational coupling is also established between the HD's stylus and the FR's TCP. This includes defining the desired relative rotation  $\mathbf{R}_{\mathcal{R}_e}^{\mathcal{H}_e}$ , and aligning manually. This is done by the human operator during what we indicate as the *engagement phase*.

The latter is presented in Section III-A1, while the human tremors filtering and the eye-hand coordination mapping, implementing the motion correspondence, are discussed in Section III-A2 and Section III-A3, respectively. The eye-hand coordination implementing the force correspondence is described in Section III-C.

1) *Engagement phase*: During the engagement phase, the EHCC retrieves the homogeneous transformation matrix of the HD's stylus  $\mathbf{T}_{\mathcal{H}_e}^{\mathcal{H}_b}(k)$ , and converts it into a robot's end-effector homogeneous transformation matrix with the following kinematic equations:

$$\mathbf{R}_{\mathcal{R}_{ed}}^{\mathcal{R}_b}(k) = \mathbf{R}_{\mathcal{H}_b}^{\mathcal{R}_b} \mathbf{R}_{\mathcal{H}_e}^{\mathcal{H}_b}(k) \mathbf{R}_{\mathcal{R}_e}^{\mathcal{H}_e}, \quad (2)$$

$$\mathbf{P}_{\mathcal{R}_{ed}}^{\mathcal{R}_b}(k) = \mathbf{P}_{\mathcal{R}_e}^{\mathcal{R}_b}(k), \quad (3)$$

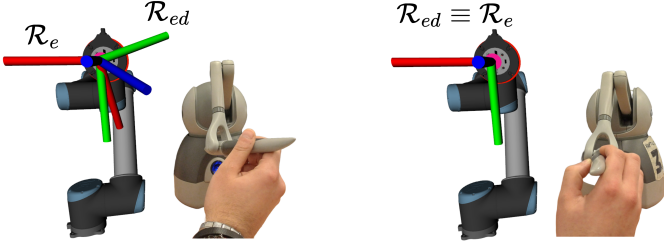


Fig. 4: Engagement phase supported by the visualization tool.

where  $\mathbf{R}_{\mathcal{H}_b}^{\mathcal{R}_b}$  is the fixed rotation between  $\mathcal{H}_b$  and  $\mathcal{R}_b$ . We note that the position of the HD's stylus is not relevant for coupling, so it is converted to the current position of the robot's TCP. The obtained frame  $\mathcal{R}_{ed}$  is real-time displayed in a visualization tool, together with the actual robot end-effector one  $\mathcal{R}_e$ , as shown in Figure 4, so that the human operator, by acting on  $\mathcal{H}_e$ , can align the frame  $\mathcal{R}_{ed}$  with the frame  $\mathcal{R}_e$ . Once the alignment is accomplished, i.e.,  $\mathbf{R}_{\mathcal{R}_b}^{\mathcal{R}_e}(k)\mathbf{R}_{\mathcal{R}_b}^{\mathcal{R}_{ed}}(k) = \mathbf{I}_3$ , the engagement phase ends, i.e., HD and FR are aligned, and the human operator can begin teleoperation.

2) *Human tremors filtering*: At each control cycle, the EHCC retrieves the actual pose  $\mathbf{x}_{\mathcal{H}_e}^{\mathcal{H}_b}(k)$  of the HD's stylus, corresponding to  $\mathbf{T}_{\mathcal{H}_e}^{\mathcal{H}_b}(k)$ . Exploiting such a pose to generate a command for the robot would result in transferring the human hand tremors, further accentuated by the control frequency. Therefore,  $\mathbf{x}_{\mathcal{H}_e}^{\mathcal{H}_b}(k)$  is filtered online by a moving average filter for poses. At the  $k$ -th control cycle, the filtered position is obtained as  $\bar{\mathbf{p}}_{\mathcal{H}_e}^{\mathcal{H}_b}(k) = \mathbf{s}(k)/m$ , where  $m \leq n$  is the number of collected samples at the  $k$ -th control cycle in the moving average window of size  $n$ , and  $\mathbf{s}(k)$  is their cumulative sum:

$$\mathbf{s}(k) = \mathbf{s}(k-1) + \mathbf{p}_{\mathcal{H}_e}^{\mathcal{H}_b}(k) - \begin{cases} 0, & \text{if } k < n; \\ \mathbf{p}_{\mathcal{H}_e}^{\mathcal{H}_b}(k-n), & \text{otherwise.} \end{cases} \quad (4)$$

The filtered quaternion  $\bar{\mathbf{q}}_{\mathcal{H}_e}^{\mathcal{H}_b}(k)$  is the eigenvector associated with the maximum eigenvalue of  $\mathbf{M}(k) = \mathbf{C}(k)/m$  [56], where  $\mathbf{C}(k)$  is the cumulative sum of samples within the window, updated at each control cycle:

$$\mathbf{C}(k) = \begin{cases} \mathbf{C}(k-1) + \mathbf{q}_{\mathcal{H}_e}^{\mathcal{H}_b}(k)[\mathbf{q}_{\mathcal{H}_e}^{\mathcal{H}_b}(k)]^\top, & \text{if } k < n; \\ \mathbf{C}(k-1) + \mathbf{q}_{\mathcal{H}_e}^{\mathcal{H}_b}(k)[\mathbf{q}_{\mathcal{H}_e}^{\mathcal{H}_b}(k)]^\top + \\ -\mathbf{q}_{\mathcal{H}_e}^{\mathcal{H}_b}(k-n)[\mathbf{q}_{\mathcal{H}_e}^{\mathcal{H}_b}(k-n)]^\top, & \text{otherwise.} \end{cases} \quad (5)$$

Keeping the cumulative sums  $\mathbf{s}(k)$  and  $\mathbf{C}(k)$  enables achieving  $\mathcal{O}(1)$  computational complexity.

3) *Eye-hand coordination*: Let  $\Delta\bar{\mathbf{p}}_{\mathcal{H}_e}^{\mathcal{H}_b}(k)$  be the HD's displacement:

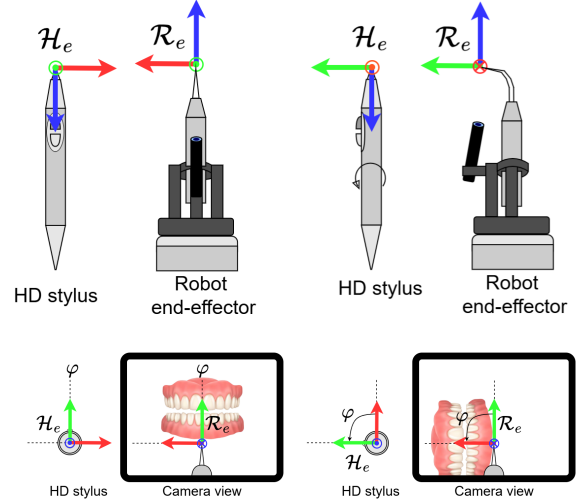
$$\Delta\bar{\mathbf{p}}_{\mathcal{H}_e}^{\mathcal{H}_b}(k) = \bar{\mathbf{p}}_{\mathcal{H}_e}^{\mathcal{H}_b}(k) - \bar{\mathbf{p}}_{\mathcal{H}_e}^{\mathcal{H}_b}(k-1), \quad (6)$$

and  $\bar{\mathbf{R}}_{\mathcal{H}_e}^{\mathcal{H}_e}(k-1)$  the relative rotation obtained from

$$\bar{\mathbf{q}}_{\mathcal{H}_e}^{\mathcal{H}_e}(k-1) = [\bar{\mathbf{q}}_{\mathcal{H}_e}^{\mathcal{H}_b}(k-1)]^\top \bar{\mathbf{q}}_{\mathcal{H}_e}^{\mathcal{H}_b}(k). \quad (7)$$

At each control cycle, the EHCC computes the HD's stylus twist:

$$\mathbf{v}_{\mathcal{H}_e}^{\mathcal{H}_b}(k) = T_s^{-1} [\Delta\bar{\mathbf{p}}_{\mathcal{H}_e}^{\mathcal{H}_b}(k)^\top, \vartheta \mathbf{r}^\top]^\top, \quad (8)$$

Fig. 5: Visualization of the rotational coupling between  $\mathcal{H}_e$  and  $\mathcal{R}_e$ : (top) top view; (bottom) user view; (left)  $\varphi = 0$ ; (right)  $\varphi = \pi/2$ .

where  $T_s \in \mathbb{R}_+$  is the control period, and  $\mathbf{r} \in \mathbb{R}^{3 \times 1}$  and  $\vartheta \in \mathbb{R}$  are the axis-angle representation corresponding to  $\bar{\mathbf{R}}_{\mathcal{H}_e}^{\mathcal{H}_e}(k-1)$ , respectively.

From (8), the corresponding desired FR's end-effector twist is obtained as:

$$\mathbf{v}_{\mathcal{R}_{ed}}^{\mathcal{R}_b}(k) = (\mathbf{I}_2 \otimes \mathbf{R}_{\mathcal{R}_b}^{\mathcal{R}_e}(k)) \left\{ \Lambda \left[ (\mathbf{I}_2 \otimes \mathbf{R}_{\mathcal{H}_e}^{\mathcal{R}_e}(k)) \cdot (\mathbf{I}_2 \otimes \mathbf{R}_{\mathcal{H}_b}^{\mathcal{H}_e}(k)) \mathbf{v}_{\mathcal{H}_e}^{\mathcal{H}_b}(k) \right] \right\}. \quad (9)$$

where  $\otimes$  denotes the Kronecker product,  $\Lambda \in \mathbb{R}^{6 \times 6}$  is the scaling diagonal matrix with  $\Lambda_{4:6,4:6} = \mathbf{I}_3$ , and

$$\mathbf{R}_{\mathcal{H}_e}^{\mathcal{R}_e}(k) = \mathbf{R}_{\mathbf{z}}^{\mathcal{R}_e}(\varphi(k)) \mathbf{R}_{\mathcal{H}_e}^{\mathcal{R}_e}. \quad (10)$$

We note that  $\mathbf{R}_{\mathcal{H}_e}^{\mathcal{R}_e}$  is the fixed rotation defining the mapping between quantities in  $\mathcal{H}_e$  and  $\mathcal{R}_e$ , and  $\mathbf{z}$  is the axis of  $\mathcal{R}_e$ , which we assume to coincide with the optical axis of the camera  $\mathbf{o}$  in  $\mathcal{R}_e$  for negligible values of the camera tilt angle. Therefore, a rotation of  $\varphi(k)$  about the  $\mathbf{z}$  axis of  $\mathcal{R}_e$  results in a viewing angle of  $\varphi(k)$ . The  $\mathbf{z}$  axis of  $\mathcal{R}_e$  is mapped to the  $\mathbf{z}$  axis of  $\mathcal{H}_e$ , according to  $\mathbf{R}_{\mathcal{H}_e}^{\mathcal{R}_e}$ . Hence, in the absence of compliance along rotational axes, the same behavior is achieved by rotating of  $\varphi(k)$  about the  $\mathbf{z}$  axis of  $\mathcal{H}_e$ , as shown in Figure 5, and (10) can be equivalently written as:

$$\mathbf{R}_{\mathcal{H}_e}^{\mathcal{R}_e}(k) = \mathbf{R}_{\mathcal{H}_e}^{\mathcal{R}_e} \mathbf{R}_{\mathbf{z}}^{\mathcal{H}_e}(\varphi(k)). \quad (11)$$

The rotation  $\mathbf{R}_{\mathcal{R}_e}^{\mathcal{R}_e}(\varphi(k))$ , or equivalently  $\mathbf{R}_{\mathbf{z}}^{\mathcal{H}_e}(\varphi(k))$ , ensures the motion correspondence between the operator's movements and those of the FR's TCP in the camera view, by appropriately rotating the desired velocities according to the viewing angle. By setting  $\mathbf{R}_{\mathcal{R}_e}^{\mathcal{R}_e}(\varphi(k)) = \mathbf{I}_3$  (or equivalently  $\mathbf{R}_{\mathbf{z}}^{\mathcal{H}_e}(\varphi(k)) = \mathbf{I}_3$ ) the mapping between twists becomes viewing angle independent:

$$\mathbf{R}_{\mathcal{H}_e}^{\mathcal{R}_e}(k) = \mathbf{R}_{\mathcal{H}_e}^{\mathcal{R}_e}, \quad \forall k \in \mathbb{N}_0. \quad (12)$$

We note that the angle  $\varphi(k)$  is obtained from the exact measurements provided by the FR's forward kinematics (or equivalently by the HD's). For this reason, even during prolonged procedures, no orientation drift is accumulated, and motion correspondence is consistently preserved.

The desired FR's TCP homogeneous transformation  $\mathbf{T}_{\mathcal{R}_{ed}}^{\mathcal{R}_b}(k)$  is obtained by numerically integrating the desired twist in (9). As for the desired rotation  $\mathbf{R}_{\mathcal{R}_{ed}}^{\mathcal{R}_b}(k)$ , it is

$$\mathbf{R}_{\mathcal{R}_{ed}}^{\mathcal{R}_b}(k) = \mathbf{R}_{\mathcal{R}_e}^{\mathcal{R}_b}(k-1)\mathbf{R}_{\mathcal{R}_{ed}(k)}^{\mathcal{R}_e(k-1)}, \quad (13)$$

where  $\mathbf{R}_{\mathcal{R}_{ed}(k)}^{\mathcal{R}_e(k-1)}$  is the rotation matrix corresponding to the axis  $\frac{\mathbf{r}}{\|\mathbf{r}\|}$  and angle  $\vartheta$ :

$$\mathbf{r} = \mathbf{R}_{\mathcal{R}_b}^{\mathcal{R}_e}(k-1)(\boldsymbol{\omega}_{\mathcal{R}_b}^{\mathcal{R}_e}(k)T_s), \quad \vartheta = \|\mathbf{r}\|. \quad (14)$$

As for the desired position  $\mathbf{p}_{\mathcal{R}_{ed}}^{\mathcal{R}_b}(k)$ , it is obtained as:

$$\mathbf{p}_{\mathcal{R}_{ed}}^{\mathcal{R}_b}(k) = \mathbf{p}_{\mathcal{R}_{ed}}^{\mathcal{R}_b}(k-1) + \dot{\mathbf{p}}_{\mathcal{R}_{ed}}^{\mathcal{R}_b}(k)T_s. \quad (15)$$

From  $\mathbf{T}_{\mathcal{R}_{ed}}^{\mathcal{R}_b}(k)$  the desired FR's TCP pose is obtained as:

$$\mathbf{x}_{\mathcal{R}_{ed}}^{\mathcal{R}_b}(k) = [\mathbf{p}_{\mathcal{R}_{ed}}^{\mathcal{R}_b}(k)^\top, \mathbf{q}_{\mathcal{R}_{ed}}^{\mathcal{R}_b}(k)^\top]^\top. \quad (16)$$

The eye-hand coordination mapping and scaling can be turned into an algorithmic procedure as described in Algorithm 1.

---

#### Algorithm 1 Eye-hand coordination mapping and scaling

---

**Input:** The HD's actual  $\bar{\mathbf{x}}_{\mathcal{H}_e}^{\mathcal{H}_b}(k)$  and previous  $\bar{\mathbf{x}}_{\mathcal{H}_e}^{\mathcal{H}_b}(k-1)$  filtered poses, and the previous desired pose  $\mathbf{x}_{\mathcal{R}_{ed}}^{\mathcal{R}_b}(k-1)$

**Output:** The desired FR's TCP pose  $\mathbf{x}_{\mathcal{R}_{ed}}^{\mathcal{R}_b}(k)$

- 1: Compute  $\mathbf{v}_{\mathcal{H}_e}^{\mathcal{H}_b}(k)$  using (8)
- 2: Compute  $\mathbf{v}_{\mathcal{R}_{ed}}^{\mathcal{R}_b}(k)$  using (9):
  - 1) Convert  $\mathbf{v}_{\mathcal{H}_e}^{\mathcal{H}_b}(k)$  into  $\mathbf{v}_{\mathcal{R}_{ed}}^{\mathcal{R}_e}(k)$  and rotate it according to the viewing angle using (10):

$$\mathbf{v}_{\mathcal{R}_{ed}}^{\mathcal{R}_e}(k) := (\mathbf{I}_2 \otimes \mathbf{R}_{\mathcal{H}_e}^{\mathcal{R}_e}(k))(\mathbf{I}_2 \otimes \mathbf{R}_{\mathcal{H}_b}^{\mathcal{H}_e}(k))\mathbf{v}_{\mathcal{H}_e}^{\mathcal{H}_b}(k)$$

- 2) Scale  $\mathbf{v}_{\mathcal{R}_{ed}}^{\mathcal{R}_e}(k)$  using  $\Lambda$  and convert it into  $\mathbf{v}_{\mathcal{R}_{ed}}^{\mathcal{R}_b}(k)$ :

$$\mathbf{v}_{\mathcal{R}_{ed}}^{\mathcal{R}_b}(k) = (\mathbf{I}_2 \otimes \mathbf{R}_{\mathcal{R}_e}^{\mathcal{R}_b}(k))(\Lambda \mathbf{v}_{\mathcal{R}_{ed}}^{\mathcal{R}_e}(k))$$

- 3: Compute  $\mathbf{T}_{\mathcal{R}_{ed}}^{\mathcal{R}_b}(k)$  from  $\mathbf{v}_{\mathcal{R}_{ed}}^{\mathcal{R}_b}(k)$  using (13) and (15)
  - 4: Extract  $\mathbf{x}_{\mathcal{R}_{ed}}^{\mathcal{R}_b}(k)$  from  $\mathbf{T}_{\mathcal{R}_{ed}}^{\mathcal{R}_b}(k)$
- 

#### B. Robot interaction control

In this section, we first formalize the contact model between the robot and the environment (Section III-B1), and subsequently, we present the free-hand strategy for limiting the interaction forces (Section III-B2) and the other safety mechanisms embedded in the controller (Section III-B3).

1) *Admittance model:* Let  $\mathbf{x}_{\mathcal{R}_{ed}}^{\mathcal{R}_b}(k)$  be the desired pose and  $\mathcal{R}_c$  the compliant frame specified by the quantities  $\mathbf{p}_{\mathcal{R}_c}^{\mathcal{R}_{ed}}(k)$ ,  $\mathbf{q}_{\mathcal{R}_c}^{\mathcal{R}_{ed}}(k)$ ,  $\mathbf{v}_{\mathcal{R}_c}^{\mathcal{R}_{ed}}(k)$ ,  $\dot{\mathbf{v}}_{\mathcal{R}_c}^{\mathcal{R}_{ed}}(k)$ . When the FR interacts with the environment,  $\mathcal{R}_c$  can be completely defined in  $\mathcal{R}_{ed}$  by integrating the mechanical impedance equation:

$$\mathbf{M}_d \ddot{\mathbf{x}}_{\mathcal{R}_c}^{\mathcal{R}_{ed}}(k) + \mathbf{K}_D \dot{\mathbf{x}}_{\mathcal{R}_c}^{\mathcal{R}_{ed}}(k) + \mathbf{K}_P \mathbf{x}_{\mathcal{R}_c}^{\mathcal{R}_{ed}}(k) = -\tilde{\mathbf{h}}^{\mathcal{R}_{ed}}(k), \quad (17)$$

where  $\mathbf{M}_d, \mathbf{K}_D, \mathbf{K}_P \in \mathbb{R}^{6 \times 6}$  are the mass, damping, and stiffness diagonal matrices, respectively, which are used to impose specific second-order mass-spring-damper dynamics;  $\tilde{\mathbf{h}}^{\mathcal{R}_{ed}}(k) = \mathbf{h}_d^{\mathcal{R}_{ed}}(k) - \mathbf{h}_e^{\mathcal{R}_{ed}}(k)$  is the wrench tracking error, defined as the difference between the desired wrench  $\mathbf{h}_d^{\mathcal{R}_{ed}}(k)$  and the exerted one  $\mathbf{h}_e^{\mathcal{R}_{ed}}(k)$ , which is equal and opposite to the measured wrench. We take  $\mathbf{h}_d^{\mathcal{R}_{ed}}(k) = \mathbf{0}, \forall k \in \mathbb{N}_0$  to make the robot behave compliantly with the environment.

2) *Free-hand force limitation strategy:* In an admittance-controlled system, the interaction wrenches emerge from the combination of the admittance parameters, the mechanical properties of the environment, and the reference provided to the controller [57]. It follows that interaction forces can be limited through a suitable reference  $\mathbf{x}_{\mathcal{R}_{ed}}^{\mathcal{R}_e}$ . Accurate limitation requires perfect knowledge of the environment that is particularly challenging to achieve, especially in a medical environment, in which the FR interacts with surfaces of varying stiffness and non-uniform geometry. Therefore, in the proposed strategy, the position reference

$$\mathbf{p}_{\mathcal{R}_{ed}}^{\mathcal{R}_e}(k) = \mathbf{R}_{\mathcal{R}_b}^{\mathcal{R}_e}(k)\mathbf{p}_{\mathcal{R}_{ed}}^{\mathcal{R}_b}(k) - \mathbf{R}_{\mathcal{R}_b}^{\mathcal{R}_e}(k)\mathbf{p}_{\mathcal{R}_e}^{\mathcal{R}_b}(k), \quad (18)$$

is dynamically scaled based solely on the contact forces:

$$\underline{\mathbf{p}}_{\mathcal{R}_{ed}}^{\mathcal{R}_e}(k) = \frac{1}{1 + K_s \|\mathbf{f}_e^{\mathcal{R}_e}(k)\|} \mathbf{p}_{\mathcal{R}_{ed}}^{\mathcal{R}_e}(k), \quad (19)$$

where  $K_s \in \mathbb{R}_+$  is a proportional gain representing a trade-off between smoothness and responsiveness of the scaling action. Indeed,  $K_s$  close to 0 reduces sudden variations of  $\underline{\mathbf{p}}_{\mathcal{R}_{ed}}^{\mathcal{R}_e}(k)$ , even in presence of noisy force measures, but provides less force-limiting action. On the other hand,  $K_s$  significantly greater than 0 makes the scaling action more responsive, but may yield oscillations in the presence of noisy measurements. Therefore, to increase the system's robustness to noisy forces, exhibiting high-frequency variations,  $\mathbf{f}_e^{\mathcal{R}_e}$  is filtered online as done for positions in (4). We note that the strategy in (19) does not allow forces to be bounded below a predefined limit. However, it prevents contact forces from growing indefinitely, ensuring a limitation even in the transients of the interaction and for any orientation of the end-effector, without relying on the knowledge of the dental environment's complex geometry.

From a control theory perspective, it is appropriate to draw an analogy between the proposed strategy and passivity-based methods, such as TDPA [49], as both rely on modulating the reference provided to the downstream controller through an adaptive damping mechanism. However, a substantial difference exists in terms of control objectives. While passivity-based approaches provide an event-triggered modulation of the reference in response to violations of the energy balance, with the explicit goal of guaranteeing system passivity, the proposed strategy implements a continuous, non-energizing, force-driven reference modulation aimed at reducing interaction forces, without relying on explicit energy estimation. As a consequence, its attenuative and smoothly varying action on the reference, resulting from an appropriate choice of the gain  $K_s$  and of the force filtering window, does not inject energy into the system, nor does it alter the underlying dynamics, in contrast to state-of-the-art variable admittance-based approaches [57], [58], which explicitly modify the controller

dynamics and typically rely on explicit knowledge of the environment [59]. As a result, the stability properties of the admittance-controlled interaction remain unaffected. Moreover, as discussed above, passivity-based control addresses an orthogonal objective to the proposed approach, and can therefore be combined with the eye–hand coordination and force limitation strategies to guarantee stability even in the presence of considerable communication delays. We consider this scenario in Section IV-B.

3) *Safety mechanisms and emergency stop protocols*: From (17) and (19), the compliant pose  $\mathbf{x}_{\mathcal{R}_c}^{\mathcal{R}_b}(k)$  to be commanded to the robot is obtained. Specifically,

$$\mathbf{p}_{\mathcal{R}_c}^{\mathcal{R}_b}(k) = \mathbf{p}_{\mathcal{R}_{ed}}^{\mathcal{R}_b}(k) + \mathbf{R}_{\mathcal{R}_{ed}}^{\mathcal{R}_b}(k)\mathbf{p}_{\mathcal{R}_c}^{\mathcal{R}_{ed}}(k), \quad (20)$$

$$\mathbf{q}_{\mathcal{R}_c}^{\mathcal{R}_b}(k) = \mathbf{q}_{\mathcal{R}_{ed}}^{\mathcal{R}_b}(k)\mathbf{q}_{\mathcal{R}_c}^{\mathcal{R}_{ed}}(k), \quad (21)$$

where  $\mathbf{x}_{\mathcal{R}_c}^{\mathcal{R}_{ed}}$ , taking the semantics of a pose error, is obtained by time-integrating  $\dot{\mathbf{v}}_{\mathcal{R}_c}^{\mathcal{R}_{ed}}$  from (17) twice. In addition to its compliant interaction properties and the embedded force limitation strategy, the controller incorporates two safety mechanisms and implements an emergency stop protocol. Regarding the safety mechanisms, the first ensures the stability of the FR in the absence of updated references from the EHCC  $\mathbf{x}_{\mathcal{R}_{ed}}^{\mathcal{R}_b}(k)$ , such as in the event of a communication loss, by continuing to track the last valid one  $\mathbf{x}_{\mathcal{R}_{ed}}^{\mathcal{R}_b}(k-1)$ . The second mechanism prevents abrupt motions of the FR by commanding  $\mathbf{x}_{\mathcal{R}_c}^{\mathcal{R}_b}(k)$  whenever the generated command  $\mathbf{x}_{\mathcal{R}_c}^{\mathcal{R}_b}(k)$  deviates excessively, either in translation or orientation, based on translational and rotational safety thresholds that can be configured by the operator according to the task requirements. With regard to the emergency stop, it focuses on the monitoring of the interaction forces. Whenever  $\|\mathbf{f}^{\mathcal{R}_e}\|(k)$  exceeds a predefined safety threshold  $f_{th}$ , the controller forwards  $\mathbf{x}_{\mathcal{R}_e}^{\mathcal{R}_b}(k)$  as the new reference while continuing to compute the admittance control law. In this way, abrupt stopping is avoided, while still allowing the interaction forces to decrease progressively.

### C. Haptic feedback controller

In performing medical procedures, the operator relies heavily on the sense of touch. Therefore, in a HBTS providing realistic haptic sensations, it becomes critical to the success of the procedures. In impedance systems, the interaction is captured by both the contact force  $\mathbf{f}_e^{\mathcal{R}_e}$  and the position error  $\tilde{\mathbf{p}}^{\mathcal{R}_e}$ , the latter being characterized by slower transients than the former, which exhibits a step dynamics. As proposed in [60], replacing  $\mathbf{f}_e^{\mathcal{R}_e}$  with  $\tilde{\mathbf{p}}^{\mathcal{R}_e} = \mathbf{p}_{\mathcal{R}_{ed}}^{\mathcal{R}_e} - \mathbf{p}_{\mathcal{R}_c}^{\mathcal{R}_e}$  to generate the force feedback makes each contact state transparent to the operator, preventing them from having to deal with sudden force changes they are not used to from previous training and fieldworks. Therefore, the proposed HFC defines a second (virtual) impedance model, generating the force feedback from the motion error of the admittance controller:

$$\mathbf{f}_h^{\mathcal{H}_b}(k) = \mathbf{K}_h \tilde{\mathbf{p}}^{\mathcal{H}_b}(k) + \mathbf{D}_h \dot{\tilde{\mathbf{p}}}^{\mathcal{H}_b}(k), \quad (22)$$

where  $\mathbf{K}_h \in \mathbb{R}^{3 \times 3}$  and  $\mathbf{D}_h \in \mathbb{R}^{3 \times 3}$  respectively are virtual stiffness and damping diagonal matrices, where

$$\begin{bmatrix} \tilde{\mathbf{p}}^{\mathcal{H}_b}(k) \\ \dot{\tilde{\mathbf{p}}}^{\mathcal{H}_b}(k) \end{bmatrix} = \left( \mathbf{I}_2 \otimes \left( \mathbf{R}_{\mathcal{H}_e}^{\mathcal{H}_b}(k) \mathbf{R}_{\mathcal{R}_c}^{\mathcal{H}_e}(k) \right) \right) \begin{bmatrix} \tilde{\mathbf{p}}^{\mathcal{R}_e}(k) \\ \dot{\tilde{\mathbf{p}}}^{\mathcal{R}_e}(k) \end{bmatrix}. \quad (23)$$

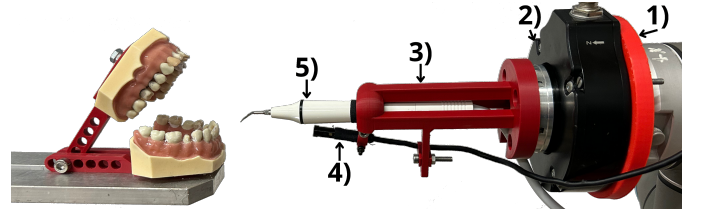


Fig. 6: Integrated mechanical end-effector for free-hand procedures. Visible in the left side of the figure is also one of the dental models used in the experiments.

We note that, as in (9), the rotation matrix  $\mathbf{R}_z^{\mathcal{R}_e}(k)$  (or equivalently  $\mathbf{R}_z^{\mathcal{H}_e}(k)$ ) in  $\mathbf{R}_{\mathcal{H}_e}^{\mathcal{R}_e}(k)$  is used to provide the force feedback correspondence with the interaction observed in the camera view. This approach is particularly suited to the considered application, as it guarantees stability while providing the operator with a natural and intuitive tactile experience that closely resembles manual execution, especially in light of Remark 2. Within this framework, the parameters  $\mathbf{K}_h$  and  $\mathbf{D}_h$  of the virtual system in (22) are tuned to shape the perceived interaction, with the stiffness matrix  $\mathbf{K}_h$  governing the transient response and the damping matrix  $\mathbf{D}_h$  contributing to vibration attenuation. Moreover, the use of a second virtual impedance model to generate the force feedback moderates the influence of transient force spikes associated with sudden contacts, while preserving informative and natural haptic feedback. We envisage the possibility that the generated feedback may exceed the range of forces that the HD device can exert. Therefore, the HFC saturates the norm of the force feedback  $\|\mathbf{f}_h^{\mathcal{H}_b}(k)\|$  to the maximum exertable force  $f_{\max}^{\mathcal{H}_b} \in \mathbb{R}_+$ :

$$\underline{\mathbf{f}}_h^{\mathcal{H}_b}(k) = \begin{cases} \mathbf{f}_h^{\mathcal{H}_b}(k), & \text{if } \|\mathbf{f}_h^{\mathcal{H}_b}(k)\| < f_{\max}^{\mathcal{H}_b}; \\ f_{\max}^{\mathcal{H}_b} \frac{\mathbf{f}_h^{\mathcal{H}_b}(k)}{\|\mathbf{f}_h^{\mathcal{H}_b}(k)\|}, & \text{otherwise.} \end{cases} \quad (24)$$

Finally, given the slow dynamics of  $\tilde{\mathbf{p}}^{\mathcal{R}_e}$ , the operator may perceive residual force even when the robot is no longer interacting. To address this, we introduce a force dead-band  $f_{db} \in \mathbb{R}_+$  to prevent the HD from reacting to such residuals:

$$\bar{\mathbf{f}}_h^{\mathcal{H}_b}(k) = \begin{cases} \underline{\mathbf{f}}_h^{\mathcal{H}_b}(k), & \text{if } \|\mathbf{f}_e^{\mathcal{R}_e}(k)\| > f_{db}; \\ \mathbf{0}, & \text{otherwise.} \end{cases} \quad (25)$$

### D. Integrated mechanical end-effector

In order to successfully perform any free-hand dental procedure, the operator relies on three basic factors: (a) the procedure-specific clinical tool; (b) the surgical field view, which may require external illumination and tools to show obstructed or poorly lit areas, e.g., a mirror; (c) the sense of touch to ensure the right pressure to be exerted on the area of interest, in order to achieve a safe and effective procedure. In this work, we design an integrated mechanical end-effector that can provide all the tools and sensory capabilities required to perform free-hand dental procedures.

With reference to Figure 6, the designed end-effector consists of five main components: (1) a *3D-printed mechanical interface* connecting the robot's flange with the force/torque

sensor; (2) a *force/torque sensor* measuring contact forces; (3) a *3D-printed tool socket* supporting the clinical tool and the endoscopic camera: the interface consists of a rigid structure to enable proper transmission of forces from the tool to the sensor, a circular hole, adjustable via a bolt-and-nut mechanism, to accommodate tools of different sizes, and a movable camera-support ring, allowing for adjustments of the view and light beam angle; (4) an *high definition endoscopic camera*, equipped with LED illumination to ensure good visibility even in poorly lit areas; (5) a *clinical tool* for performing the procedure of interest: the tool is placed in the supporting socket after being wrapped with friction tape to ensure good mechanical compliance, emulating the skin friction between the operator’s hand and the tool; the tool used for the chosen use case is a scaler.

Although the current implementation does not fulfill yet all clinical requirements, such a design is compatible with future clinical adoption, as the end-effector is inherently compatible with standard sterilization and infection-control procedures commonly adopted in dentistry. Indeed, clinical instruments are intrinsically designed to withstand autoclave sterilization, and the literature reports the availability of sterilizable endoscopic cameras [61], as well as autoclavable or low-temperature-sterilizable materials, including medical-grade 3D-printed polymers, which would enable full sterilization of the entire assembly [62]. Moreover, the tool socket has been designed with smooth external surfaces and a reduced number of crevices, thereby facilitating cleaning and reprocessing. In addition, the socket enables rapid tool replacement by simple extraction and insertion of the clinical instrument, without requiring disassembly of the end-effector or disconnection of sensing and vision components. Components upstream of the end-effector, such as the force/torque sensor and the robot flange, which are not compatible with autoclave sterilization, can be isolated using sterile drapes or disposable sterile barriers, as commonly adopted in medical robotic systems [63]. With respect to aerosol management, a critical concern in dental procedures such as SRP, the proposed design does not interfere with conventional mitigation strategies. In a clinical deployment, aerosol generation could be managed through standard high-volume evacuation systems and saliva ejectors, without requiring any modification to the design.

#### IV. TECHNICAL VALIDATION

To evaluate the performance of the proposed FH-HBTS, we conduct a set of experiments including static force application (Section IV-B), dynamic dental scaling motions (provided in the supplementary materials), and a free-space experiment (Section IV-C). During the experiments, the robot is out of the operator’s view, who relies solely on the visual feedback from the camera and the force feedback from the HD. We select three target teeth: the lower right first premolar, the upper right central incisor, and the upper right second premolar. The chosen targets are significant as each requires a different tool orientation, making the use of eye-hand coordination essential.

#### A. Experimental setup

The experimental setup involves the following equipment and materials: (I) a leader control station featuring a 6-degrees-of-freedom (DOF) force-feedback HD<sup>2</sup> and a workstation: the latter is a general purpose computer executing the leader controller loop, and communicating with the FR over an Ethernet network, where delays and packet losses are negligible; (II) a FR consisting of the 6-DOF UR10 arm<sup>3</sup>, equipped with the integrated mechanical end-effector of Section III-D, where the force/torque sensor is the Robotiq FT150<sup>4</sup>; (III) a high-strength resin dental model and a 3D-printed dental phantom, both life-sized models of a human mouth. The former is used for the experiments described in this section, while the latter only appears in the accompanying video.

#### B. Force limitation assessment

To assess the effectiveness of the proposed force limitation strategy, we perform 9 interaction experiments, with an average duration of  $\sim 20$  s each, 3 for each target tooth, without force limitation (Scenario A), 9 more with force limitation (Scenario B) and 9 with a passivity-based architecture (Scenario C), specifically TDPA-HD, where admittance control replaces Cartesian impedance control adopted in [47]. In the latter scenario, the force limitation is intentionally kept disabled in order to isolate the effects of TDPA-HD. For each scenario, we record the data sequence  $\{a(k), b(k)\}_{k=1}^N$ , sampling at a frequency of 125 Hz, where we set the force norm  $\|\mathbf{f}_e^{\mathcal{R}_e}(k)\|$  as  $a(k) \in \mathcal{A} \subseteq \mathbb{R}_+$ , and the commanded virtual penetration  $\|\mathbf{p}_{\mathcal{R}_{ed}}^{\mathcal{R}_e}(k)\|$  as  $b(k) \in \mathcal{B} = \{b \in \mathbb{R} | b_{\min} = 0 \text{ m} \leq b \leq b_{\max} = 0.007 \text{ m}\}$ . We discretize  $\mathcal{B}$  with the step  $b_{\text{step}} = 0.0001 \text{ m}$ , selected based on the repeatability of the FR, while  $b_{\max}$  is the maximum virtual penetration observed across all experiments.

By binning data in  $\mathcal{B}$ , following [64], we estimate the conditional expectation of the exerted force  $E(\|\mathbf{f}_e^{\mathcal{R}_e}\| | \|\mathbf{p}_{\mathcal{R}_{ed}}^{\mathcal{R}_e}\|)$  and the conditional standard deviation, obtained as the square root of the conditional variance  $\text{Var}(\|\mathbf{f}_e^{\mathcal{R}_e}\| | \|\mathbf{p}_{\mathcal{R}_{ed}}^{\mathcal{R}_e}\|)$ , in all three scenarios. Visual inspection of Figure 7 showcases a significant reduction in the expected interaction force in Scenario B, given the same commanded virtual penetration. Notably, TDPA-HD [47] (Scenario C) cannot reduce the interaction force in quasi-static contacts due to the energy being approximately zero.

To evaluate the effectiveness of the force limitation strategy, we compare  $E(\|\mathbf{f}_e^{\mathcal{R}_e}\| | \|\mathbf{p}_{\mathcal{R}_{ed}}^{\mathcal{R}_e}\|)$  and  $\text{Var}(\|\mathbf{f}_e^{\mathcal{R}_e}\| | \|\mathbf{p}_{\mathcal{R}_{ed}}^{\mathcal{R}_e}\|)$  in all three scenarios. We assess differences in conditional variances through Levene’s and Bartlett’s tests in the comparisons involving Scenario B, i.e., B–A and B–C. Both tests indicate significantly different variances ( $p \approx 0$ ), showing that the force limitation strategy affects the dispersion of the force norm  $\|\mathbf{f}_e^{\mathcal{R}_e}(k)\|$  with respect to virtual penetration  $\|\mathbf{p}_{\mathcal{R}_{ed}}^{\mathcal{R}_e}(k)\|$ . Since Levene’s test suggests a significant variance difference, we apply Welch’s t-test, which is more robust in the case of unequal variances. In the B–A comparison, the test yields a

<sup>2</sup><https://www.3dsystems.com/haptics-devices/touch>

<sup>3</sup><https://www.universal-robots.com/>

<sup>4</sup><https://robotiq.com>

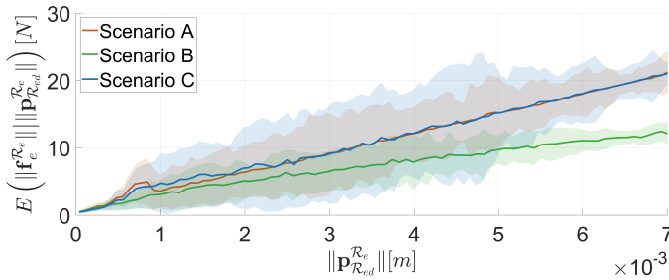


Fig. 7: Comparison between the conditional expectation of the interaction force in all three scenarios.

t-statistic  $t = -4.52$  with  $p \approx 0$ , confirming a statistically significant force reduction in Scenario B. Beyond statistical significance, the magnitude of this effect is notable: the comparison yields a Cohen's  $d = -0.63$ , indicating a significant force reduction when the force limitation strategy is enabled. The corresponding confidence interval  $[-0.91, -0.36]$  does not include zero, further supporting the robustness and consistency of the observed effect across the explored range of virtual penetration.

An analogous analysis is conducted for the B-C comparison. Also in this case, Welch's t-test confirms a statistically significant reduction of the normal force with respect to Scenario C ( $p \approx 0$ ), indicating that the force limitation strategy yields lower contact forces than the passivity-based control architecture. The observed effect is comparable in magnitude to that of the B-A comparison (Cohen's  $d = -0.68$  and confidence interval  $[-0.97, -0.41]$ ), further supporting the robustness of the proposed approach across different control architectures.

### C. Eye-hand coordination assessment

To perform a formal assessment of eye-hand coordination, we execute a teleoperated task in the free space. The operator performs a translatory motion with the HD, simultaneously rotating the viewing angle by rotating the HD's stylus by an angle  $\varphi$  about the z axis of  $\mathcal{H}_e$ . The validation is considered completed if the motion transferred to the robot varies as the viewing angle does. Figure 8 shows the  $\varphi$  angle, the position of HD's stylus and the position of the FR, respectively.

Results showcase that, as long as the angle  $\varphi = 0$  rad (from 0s to 10s), a motion along the x axis of  $\mathcal{H}_b$  is mapped into a motion along the x axis of  $\mathcal{R}_b$ . When the angle turns into  $\varphi = -\pi/2$  rad, a motion along the x axis of  $\mathcal{H}_b$  is mapped into a motion along the z axis of  $\mathcal{R}_b$  (from 20s to 30s).

These results confirm that the mapping of motion between HD space and FR space is affected by the rotation of the visual field. However, they do not provide any suggestion regarding the effectiveness of eye-hand coordination for the human operator. Therefore, in the accompanying video we provide a comprehensive qualitative assessment of the latter.

## V. IN-VITRO PRE-CLINICAL VALIDATION

To validate the feasibility of the FH-HBTS in performing free-hand dental procedures, we conduct an in-vitro experimental trial replicating a SRP procedure under more representative clinical conditions. The procedure is carried out

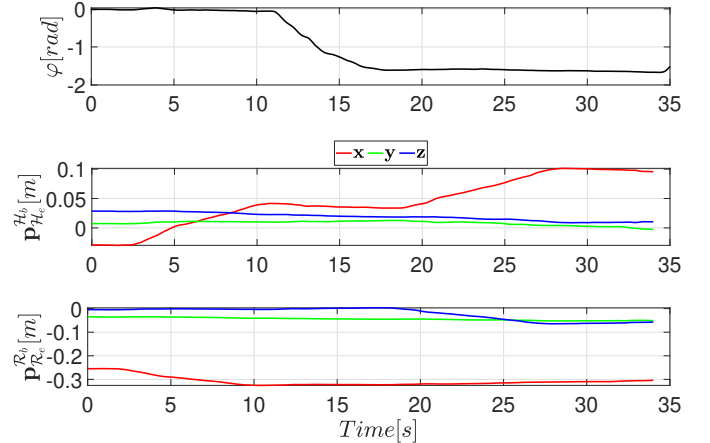


Fig. 8: Eye-hand coordination assessment.

on the dental model, coated with an acrylic polymer-based suspension containing titanium dioxide to simulate artificial calculus, using a fully functional ultrasonic scaler activated via a foot pedal at the leader control station.

A total of 20 participants with varying levels of experience in the dental field are recruited: (*Group 1*) dental students who had performed at least 20 in-vivo dental scaling procedures (31.6%); (*Group 2*) dentists with less than 5 years of professional experience (36.8%); (*Group 3*) dentists with more than 5 years of professional experience (31.6%). Before the experimental phase, all participants complete a structured training session aimed at ensuring competent use of the system, during which they practice approaching the dental surface, maintaining stable contact, and performing preliminary calculus removal.

After training, participants perform artificial calculus removal on selected tooth surfaces: lower left central incisor, lower left second molar, lower right first molar, relying on both visual and haptic feedback. For each trial, each surface is uniformly coated with a thin layer of artificial calculus. The procedure is considered successful if the participant is satisfied with the outcome and none of the safety mechanisms described in Section III-B3 are triggered. A single representative trial, illustrating the overall experimental procedure, is provided in the accompanying video.

### A. Data collection and analysis

To comprehensively evaluate system performance, operator experience, and operational safety, a set of objective and subjective outcome measures is collected and analyzed. These include indicators of clinical efficacy, task efficiency, interaction safety, and perceived workload and usability. Differences across participant experience levels are assessed for all outcome measures using Kruskal-Wallis tests.

System efficacy is evaluated by an independent expert dentist, who assesses calculus removal using a six-point ordinal scale ranging from no removal to complete removal. Task efficiency is quantified through the median execution time per dental surface, while interaction safety is assessed by analyzing the magnitude of the interaction forces exerted

during the procedure. Both metrics are compared with reference values reported in the literature for manual execution. Finally, system usability is evaluated through subjective measures, including the NASA-Task Load Index (NASA-TLX) questionnaire for perceived workload, the System Usability Scale (SUS) questionnaire for usability, and additional 5-point Likert-scale questions to further characterize the operator interaction. The complete questionnaire is reported in the supplementary materials.

### B. Results

All participants were able to successfully complete the entire experimental procedure. Regarding system efficacy, the mean cleanliness score per participant, averaged over the three teeth, ranges from a minimum of 3.66 to a maximum of 4.28, indicating a generally high and homogeneous level of task execution. No statistically significant differences between groups are observed, as confirmed by the Kruskal–Wallis test conducted at a significance level of  $p = 0.05$ .

Regarding execution time, the duration of the procedure per tooth showcases substantial variability, ranging from 85 s to 212 s. The median execution times are 153.5 s for Group 1, 162.0 s for Group 2, and 147.5 s for Group 3. Reference values reported in [65] for manual performance of the same procedure indicate a median execution time of 115.5 s. Although the teleoperated procedure is therefore slower than manual execution, participants exhibited an average reduction of 20.4% in completion time in the second trial, followed by a further 23.2% reduction in the third trial. This trend reflects a clear learning-curve effect, indicating that operators progressively familiarize themselves with the system and improve their ability to control the remote tool. This suggests that, with more extensive training, teleoperated performance could gradually approach manual execution levels.

In terms of interaction forces, during the experimental trial, the force magnitude results in an overall mean of  $1.78 \pm 0.19$  N for Group 1,  $1.86 \pm 0.34$  N for Group 2, and  $1.96 \pm 0.32$  N for Group 3, with average maximum peaks of  $9.44 \pm 3.09$  N,  $9.80 \pm 4.7$  N, and  $11.47 \pm 4.41$  N, respectively. When comparing groups, Kruskal–Wallis tests find no statistically significant differences between experience levels. The comparison with reference values reported in the literature for dentists performing the procedure free-hand highlights a clear discrepancy. In particular, [66] reports an average interaction force of  $0.28 \pm 0.33$  N, with average maximum peaks of approximately 0.60 N. These values are close to the tissue safety thresholds reported in the literature for dental procedures, commonly identified at around 0.5 N [67]. Notably, these reference values are also compatible with those measured in a dedicated free-hand SCP procedure we conduct on the dental model mounted on the force/torque sensor to directly measure interaction forces. Further details on this experiment are provided in the supplementary materials. This difference reflects an inherent limitation of the system, which is primarily attributable to the mechanical characteristics of the adopted industrial robot and to the resolution of the force/torque sensor, not specifically designed to accurately manage the low-magnitude forces typical of dental interactions. Despite the higher measured forces,

	Group 1	Group 2	Group 3	K–W test	
	Mean $\pm$ STD	Mean $\pm$ STD	Mean $\pm$ STD	$\chi^2$	p
<b>NASA-TLX</b>					
Mental Demand	30.00 $\pm$ 27.57	51.43 $\pm$ 15.74	36.67 $\pm$ 23.38	2.91	0.23
Physical Demand	26.67 $\pm$ 24.22	20.00 $\pm$ 11.55	16.67 $\pm$ 19.66	0.70	0.70
Temporal Demand	36.67 $\pm$ 23.38	42.86 $\pm$ 13.80	36.67 $\pm$ 15.06	0.52	0.77
Performance	43.33 $\pm$ 8.17	37.14 $\pm$ 13.80	33.33 $\pm$ 10.33	2.42	0.30
Effort	16.67 $\pm$ 19.66	8.57 $\pm$ 10.69	23.33 $\pm$ 15.06	2.79	0.25
Frustration	30.00 $\pm$ 27.57	28.57 $\pm$ 27.95	33.33 $\pm$ 16.33	0.11	0.94
Overall	26.19 $\pm$ 18.65	26.94 $\pm$ 13.36	25.71 $\pm$ 14.26	2.00	0.37
<b>SUS</b>	77.92 $\pm$ 13.46	81.07 $\pm$ 9.11	78.75 $\pm$ 10.34	0.51	0.78
<b>5-point Likert Scale</b>					
Ergonomics	3.83 $\pm$ 0.75	3.71 $\pm$ 0.76	4.17 $\pm$ 0.98	0.95	0.62
Fidelity	3.17 $\pm$ 1.33	3.00 $\pm$ 0.58	3.33 $\pm$ 0.52	0.87	0.65
Motion correspondence	4.17 $\pm$ 0.41	4.00 $\pm$ 0.82	4.33 $\pm$ 0.82	0.78	0.68
Force correspondence	4.00 $\pm$ 0.89	4.14 $\pm$ 0.38	4.17 $\pm$ 0.75	0.17	0.92
Depth perception	2.17 $\pm$ 0.98	1.71 $\pm$ 0.76	2.33 $\pm$ 0.52	2.19	0.33
Interaction events	3.83 $\pm$ 0.98	3.43 $\pm$ 0.98	4.00 $\pm$ 1.10	1.30	0.52
Interaction effects	3.83 $\pm$ 0.98	3.43 $\pm$ 0.79	4.17 $\pm$ 0.75	2.73	0.26
Feedback naturalness	4.00 $\pm$ 0.89	3.71 $\pm$ 0.95	3.83 $\pm$ 1.17	0.33	0.85

TABLE I: Summary of the NASA-TLX and 5-point Likert scale questionnaire responses and SUS scores.

no superficial damage was observed on the dental model, suggesting that the system remains safe under the adopted experimental conditions. However, these results should be regarded as scalable, as the interaction forces are strongly influenced by the employed hardware setup and are expected to decrease when adopting an engineered system tailored to the target application, particularly in terms of mechanical compliance and force/torque sensing resolution.

The results of the Kruskal–Wallis tests on questionnaire responses are reported in Table I. No statistically significant differences emerge across any NASA-TLX dimension, SUS score, or 5-point Likert item ( $p > 0.05$ ), indicating that subjective evaluations are consistent across experience levels. Across all groups, the NASA-TLX results indicate a consistently moderate perceived workload, with contained mental, physical, and temporal demands, limited variability in performance ratings, and generally low effort and frustration. Overall, the task is perceived as manageable and not overly demanding. System usability is evaluated positively, with SUS scores falling within the good-usability range [68], confirming that the system is considered intuitive and easy to use. Likert-scale evaluations further highlight high ratings for interaction-related aspects, including motion and force correspondence, first contact and prolonged interaction perception, and the naturalness of the haptic feedback (mean  $\in [3.43, 4.33]$ ), suggesting coherent and supportive sensory feedback. Ergonomics is also positively evaluated (mean  $\in [3.71, 4.17]$ ), exceeding the manual reference condition of 3 and indicating improved ergonomic and postural comfort during teleoperation. Fidelity achieves only moderately positive scores, likely due to limitations in depth perception (mean  $\in [1.71, 2.33]$ ), preventing accurate situational awareness.

## VI. CONCLUSIONS AND FUTURE PERSPECTIVES

This paper proposed a FH-HBTS for free-hand dental procedures. The system features visual and haptic feedback, that are appropriately combined and coordinated to allow for a natural teleoperation experience. To improve the visibility of the intervention site, we designed a dedicated end-effector accommodating an eye-in-hand endoscopic camera, and ensuring compatibility with existing clinical tools. We also improved

the accuracy of the procedure by introducing human tremor filtering and dynamic scaling of velocities. Through eye-hand coordination and TCP control, we enabled the operator to perceive the motion correspondence between their movements and those of the end-effector, observed in the camera view, preserving manual dexterity and expertise. Additionally, by appropriately transforming the virtualized force feedback, we also ensured the force correspondence, enabling the human operator to experience a highly natural sensory perception. Finally, we enabled safe interactions by scaling the motion references provided to the admittance controller. The proposed strategy allows for accurate force limitation in any contact state and for any orientation of the interaction tool, without requiring any prior modeling of the intervention site.

We believe that our FH-HBTS represents a crucial step towards a broader adoption of robotics in dentistry, as it allows for accurate treatments, while preserving the operator's cognitive and technical abilities. With respect to manual procedures, our system allows improving operator's ergonomics, tracking operator's performance, and perspective enabling remote healthcare.

We emphasize that the proposed system allows collecting haptic and motion data. While this feature is crucial during the training phase of new operators for the evaluation of learning metrics, i.e. learning curves [69], it is also central towards the deployment of data-driven control architectures that leverage demonstrations to synthesize autonomous control policies [70]. Finally, these data can also be used to learn cost functions [71], and hence intentions, of experts fulfilling a given task. In the context of dental procedures, this means that data collected from experts executing the procedure can be used to train policies for autonomous robots.

With our future work we plan to extend the FH-HBTS with autonomous patient motion compensation to further enhance system's safety and flexibility, and to benchmark the performance against the da Vinci Surgical System<sup>TM</sup>. In addition, future experimental testbeds will be designed to progressively incorporate clinically relevant sources of complexity that are not yet addressed in the present study, including constrained inter-proximal access, interaction with soft tissues, fluid presence, and limited workspace conditions. In this context, we plan to collect expert demonstrations for the development of (semi-)autonomous dental procedures. Beyond algorithmic extensions, a key direction of future work concerns the evolution of the experimental platform itself, which will be redesigned towards a fully engineered, application-driven system, explicitly accounting for the mechanical, sensing, and ergonomic requirements of dental procedures, and addressing the hardware-related limitations identified in the present study.

#### ACKNOWLEDGMENTS

The authors would like to thank X for their assistance during the in-vitro pre-clinical validation and Y for supporting the EHCC implementation and end-to-end system validation, making this work possible.

#### REFERENCES

- [1] J. Grischke, L. Johannsmeier, L. Eich, L. Griga, and S. Haddadin, "Dentronics: Towards robotics and artificial intelligence in dentistry," *Dent. Mater.*, vol. 36, no. 6, pp. 765–778, Jun. 2020.
- [2] A. Podhorsky, P. Rehmann, and B. Wöstmann, "Tooth preparation for full-coverage restorations—a literature review," *Clin. Oral Invest.*, vol. 19, no. 5, pp. 959–968, Jun. 2015.
- [3] M. Sanz, D. Herrera, M. Kebschull, I. Chapple, S. Jepsen, T. Berglundh, A. Sculean, M. S. Tonetti, and EFP Workshop Participants and Methodological Consultants, "Treatment of stage i–III periodontitis—the EFP s3 level clinical practice guideline," *J. Clin. Periodontol.*, vol. 48, no. 1, pp. 4–60, Jan. 2021.
- [4] A. Afshari, R. Shahmohammadi, S. A. Mosaddad, O. Pesteei, E. Hajmohammadi, M. Rahbar, M. Alam, and K. Abbasi, "Free-Hand versus Surgical Guide Implant Placement," *Adv. Mater. Sci. Eng.*, vol. 2022, no. 1, p. 6491134, Feb. 2022.
- [5] A. Kozlovsky, A. Rapaport, and Z. Artzi, "Influence of operator skill level on the clinical outcome of non-surgical periodontal treatment: a retrospective study," *Clin. Oral Invest.*, vol. 22, no. 8, pp. 2927–2932, Nov. 2018.
- [6] J. Y. N. Luo, P. P. Liu, and M. C. M. Wong, "Patients' satisfaction with dental care: a qualitative study to develop a satisfaction instrument," *BMC Oral Health*, vol. 18, no. 1, p. 15, Jan. 2018.
- [7] S. Schnutenhaus, M. Wagner, C. Edelmann, R. G. Luthardt, and H. Rudolph, "Factors Influencing the Accuracy of Freehand Implant Placement: A Prospective Clinical Study," *Dent. J.*, vol. 9, no. 5, p. 54, May 2021.
- [8] S. Y. Soo, W. S. Ang, C. H. Chong, I. M. Tew, and N. A. Yahya, "Occupational ergonomics and related musculoskeletal disorders among dentists: A systematic review," *Work*, vol. 74, no. 2, pp. 469–476, 2023.
- [9] A. Gupta, M. Bhat, T. Mohammed, N. Bansal, and G. Gupta, "Ergonomics in dentistry," *Int. J. Clin. Pediatr. Dent.*, vol. 7, no. 1, pp. 30–34, Apr. 2014.
- [10] J. Field, J. Dixon, A. Towers, R. Green, H. Albagami, G. Lambourn, J. Mallinson, W. Fokkinga, J. Tricio-Pesce, T. Crnić, and S. Vital, "Defining dental operative skills curricula: An ADEE consensus paper," *Eur. J. Dent. Educ.*, vol. 25, no. 2, pp. 405–414, May 2021.
- [11] E. L. McGleenon and S. Morison, "Preparing dental students for independent practice: a scoping review of methods and trends in undergraduate clinical skills teaching in the UK and Ireland," *Br. Dent. J.*, vol. 230, no. 1, pp. 39–45, Jan. 2021.
- [12] K. Uoshima, N. Akiba, and M. Nagasawa, "Technical skill training and assessment in dental education," *Jpn. Dent. Sci. Rev.*, vol. 57, pp. 160–163, Nov. 2021.
- [13] H. L. Abouzeid, S. Chaturvedi, K. M. Abdelaziz, F. A. Alzahrani, A. A. S. Al-Qarni, and N. M. Alqahtani, "Role of robotics and artificial intelligence in oral health and preventive dentistry - knowledge, perception and attitude of dentists," *Oral Health Prev. Dent.*, vol. 19, pp. 353–363, Jul. 2021.
- [14] G. Raju, G. Verghese, and T. Sheridan, "Design issues in 2-port network models of bilateral remote manipulation," in *Proc. Int. Conf. Rob. Autom.*, May 1989, pp. 1316–1321.
- [15] R. Yasin, P. Chalasani, N. Zevallos, M. Shahbazi, Z. Li, A. Deguet, P. Kazanzides, H. Choset, R. H. Taylor, and N. Simaan, "Evaluation of hybrid control and palpation assistance for situational awareness in telemanipulated task execution," *IEEE Trans. Med. Rob. Bionics*, vol. 3, no. 1, pp. 31–43, Feb. 2021.
- [16] D. Kundrat, A. Schoob, T. Piskorn, R. Grässlin, P. J. Schuler, T. K. Hoffmann, L. A. Kahrs, and T. Ortmaier, "Toward assistive technologies for focus adjustment in teleoperated robotic non-contact laser surgery," *IEEE Trans. Med. Rob. Bionics*, vol. 1, no. 3, pp. 145–157, Aug. 2019.
- [17] Z. Deng, X. Wei, C. Pan, G. Li, and Y. Hu, "Shared control of tendon-driven continuum robots using visibility-guaranteed optimization for endoscopic surgery," *IEEE Trans. Med. Rob. Bionics*, vol. 6, no. 2, pp. 487–497, May 2024.
- [18] A. Y. Alqutaibi, H. H. Hamadallah, B. Abu zaid, A. M. Aloufi, and R. A. Tarawah, "Applications of robots in implant dentistry: A scoping review," *J. Prosthet. Dent.*, Dec. 2023.
- [19] Y. Wu, S. Zou, P. Lv, and X. Wang, "Accuracy of an autonomous dental implant robotic system in dental implant surgery," *J. Prosthet. Dent.*, vol. 133, no. 3, pp. 764–770, Aug. 2024.
- [20] H. S. Talib, G. N. Wilkins, and I. Turkyilmaz, "Flapless dental implant placement using a recently developed haptic robotic system," *Br. J. Oral Maxillofac. Surg.*, vol. 60, no. 9, pp. 1273–1275, Nov. 2022.

- [21] Y. Kasahara, H. Kawana, S. Usuda, and K. Ohnishi, "Telerobotic-assisted bone-drilling system using bilateral control with feed operation scaling and cutting force scaling," *Int. J. Med. Rob. Comput. Assisted Surg.*, vol. 8, no. 2, pp. 221–229, Jun. 2012.
- [22] P. Ahmad, M. K. Alam, A. Aldajani, A. Alahmari, A. Alanazi, M. Stoddart, and M. G. Sghaireen, "Dental robotics: A disruptive technology," *Sensors*, vol. 21, no. 10, p. 3308, Jan. 2021.
- [23] J. Jiang, Y. Guo, Z. Huang, Y. Zhang, D. Wu, and Y. Liu, "Adjacent surface trajectory planning of robot-assisted tooth preparation based on augmented reality," *Eng. Sci. Technol. Int. J.*, vol. 27, p. 101001, Mar. 2022.
- [24] L. Wang, D. Wang, L. Ma, Y. Zhang, F. Yuan, Y. Sun, and P. Lv, "Preliminary experiments of a miniature robotic system for tooth ablation using ultra-short pulsed lasers," in *Proc. IEEE/RSI Int. Conf. Intell. Robots Syst.*, 2013, pp. 2566–2571.
- [25] L. Wang, D. Wang, Y. Zhang, L. Ma, Y. Sun, and P. Lv, "An automatic robotic system for three-dimensional tooth crown preparation using a picosecond laser," *Lasers Surg. Med.*, vol. 46, no. 7, pp. 573–581, 2014.
- [26] L. Ma, Y. Zhang, D. Wang, P. Lv, Y. Sun, and H. Wang, "Trajectory tracking control of a miniature laser manipulation robotic end-effector for dental preparation," in *Proc. IEEE Int. Conf. Rob. Biomim.*, Dec. 2013, pp. 468–473.
- [27] F. Yuan and P. Lyu, "A preliminary study on a tooth preparation robot," *Adv. Appl. Ceram.*, vol. 119, no. 5, pp. 332–337, 2020.
- [28] Y. Zhang, Z. Zhao, R. Song, J. Lu, P. Lu, and Y. Wang, "Tooth arrangement for the manufacture of a complete denture using a robot," *Ind. Robot*, vol. 28, no. 5, pp. 420–425, Oct. 2001.
- [29] T. Otani, A. J. Raigrodski, L. Mancl, I. Kanuma, and J. Rosen, "In vitro evaluation of accuracy and precision of automated robotic tooth preparation system for porcelain laminate veneers," *J. Prosthet. Dent.*, vol. 114, no. 2, pp. 229–235, Aug. 2015.
- [30] F. Yuan, Y. Wang, Y. Zhang, Y. Sun, D. Wang, and P. Lyu, "An automatic tooth preparation technique: A preliminary study," *Sci. Rep.*, vol. 6, p. 25281, Apr. 2016.
- [31] J. Dong and H. Everett, "The development of endodontic micro robot," in *Proc. ASME Int. Mech. Eng. Congr. Expo.*, May 2009, pp. 201–204.
- [32] J. Dong and S. Y. Hong, "Design of z axis actuator and quick tool change assembly for an endodontic micro robot," in *Proc. ASME Int. Mech. Eng. Congr. Expo.*, 2012, pp. 507–511.
- [33] G. Hwang, A. J. Paula, E. E. Hunter, Y. Liu, A. Babeer, B. Karabucak, K. Stebe, V. Kumar, E. Steager, and H. Koo, "Catalytic antimicrobial robots for biofilm eradication," *Sci. Rob.*, vol. 4, no. 29, 2019.
- [34] T. Gulrez, A. K. Shahid, U. Sana, and N. G. Chaudhary, "Visual guided robotic endodontic therapeutic system," in *Proc. Int. Conf. Inf. Emerging Technol.*, Jun. 2010, pp. 1–6.
- [35] L. Liu, M. Watanabe, and T. Ichikawa, "Robotics in dentistry: A narrative review," *Dent. J.*, vol. 11, no. 3, p. 62, Feb. 2023.
- [36] O. S. Ajani and S. F. M. Assal, "Hybrid force tracking impedance control-based autonomous robotic system for tooth brushing assistance of disabled people," *IEEE Trans. Med. Rob. Bionics*, vol. 2, no. 4, pp. 649–660, Nov. 2020.
- [37] T. C. T. van Riet, K. T. H. Chin Jen Sem, J.-P. T. F. Ho, R. Spijker, J. Kober, and J. de Lange, "Robot technology in dentistry, part two of a systematic review: an overview of initiatives," *Dent. Mater.*, vol. 37, no. 8, pp. 1227–1236, 2021.
- [38] Z. Xia, F. Ahmad, H. Deng, L. Jiang, W. Qin, Q. Zhao, and J. Xiong, "Robotics application in dentistry: A review," *IEEE Trans. Med. Rob. Bionics*, vol. 6, no. 3, pp. 851–867, 2024.
- [39] Y. Li, Y. Inamochi, Z. Wang, and K. Fueki, "Clinical application of robots in dentistry: A scoping review," *J. Prosthodont. Res.*, vol. 68, no. 2, pp. 193–205, 2023.
- [40] H. Ravichandar, A. S. Polydoros, S. Chernova, and A. Billard, "Recent advances in robot learning from demonstration," *Annu. Rev. Control Rob. Auton. Syst.*, vol. 3, no. 1, pp. 297–330, 2020.
- [41] M. Li, Y.-H. Liu, and Q. Huang, "An optimized haptic interaction model based on support vector regression for evaluation of endodontic shaping skill," in *Proc. IEEE Int. Conf. Rob. Biomim.*, 2007, pp. 617–622.
- [42] M. N. Milner, E. C. Anania, K. Candelaria-Oquendo, S. Rice, S. R. Winter, and N. K. Ragbir, "Patient perceptions of new robotic technologies in clinical restorative dentistry," *J. Med. Syst.*, vol. 44, no. 2, 2019.
- [43] G. Niemeyer, C. Preusche, S. Stramigioli, and D. Lee, "Telerobotics," in *Springer Handb. Rob.*, 2016, pp. 1085–1108.
- [44] I. Aliaga, A. Rubio, and E. Sanchez, "Experimental quantitative comparison of different control architectures for master-slave teleoperation," *IEEE Trans. Control Syst. Technol.*, vol. 12, no. 1, pp. 2–11, Jan 2004.
- [45] K. Hashtrudi-Zaad and S. E. Salcudean, "Analysis of control architectures for teleoperation systems with impedance/admittance master and slave manipulators," *Int. J. Rob. Res.*, vol. 20, no. 6, pp. 419–445, Jun 2001.
- [46] K. Razi and K. Hashtrudi-Zaad, "Extension of zeheb-walach absolute stability criteria for robot-human interactions," in *Proc. IEEE Conf. Decis. Control*, Dec 2012, pp. 1186–1191. [Online]. Available: <https://ieeexplore.ieee.org/document/6426356>
- [47] M. Panzirsch, A. Pereira, H. Singh, B. Weber, E. Ferreira, A. Gherghescu, L. Hann, E. den Exter, F. van der Hulst, L. Gerdes, L. Cencetti, K. Wormnes, J. Grenouilleau, W. Carey, R. Balachandran, T. Hulin, C. Ott, D. Leidner, A. Albu-Schäffer, N. Y. Lii, and T. Krüger, "Exploring planet geology through force-feedback telemanipulation from orbit," *Sci. Rob.*, vol. 7, no. 65, Apr. 2022.
- [48] M. Salehi and A.-A. Ahmadi, "Improvement in the conservatism of the time domain passivity approach in delayed position-position teleoperation system," *Int. J. Intell. Rob. Appl.*, vol. 8, no. 3, pp. 619–628, Sep. 2024.
- [49] J. Artigas, J.-H. Ryu, and C. Preusche, "Time domain passivity control for position-position teleoperation architectures," *Presence*, vol. 19, no. 5, pp. 482–497, Oct. 2010.
- [50] G. Flandin, F. Chaumette, and E. Marchand, "Eye-in-hand/eye-to-hand cooperation for visual servoing," in *Proc. IEEE Int. Conf. Rob. Autom.*, Apr. 2000, pp. 2741–2746.
- [51] M. Radi, "Workspace Scaling and Haptic Feedback for Industrial Telepresence and Teleaction Systems with Heavy-duty Teleoperators," in *Forschungsberichte IWB*, 2012.
- [52] F. Conti and O. Khatib, "Spanning large workspaces using small haptic devices," in *Proc. IEEE World Haptics Conf.*, Mar. 2005, pp. 183–188.
- [53] S. E. Salcudean, M. Zhu, W.-H. Zhu, and K. Hashtrudi-Zaad, "Transparent bilateral teleoperation under position and rate control," *Int. J. Rob. Res.*, vol. 19, no. 12, pp. 1185–1202, Dec. 2000.
- [54] C. Freschi, V. Ferrari, F. Melfi, M. Ferrari, F. Mosca, and A. Cuschieri, "Technical review of the da vinci surgical telemanipulator," *Int. J. Med. Rob. Comput. Assisted Surg.*, vol. 9, no. 4, pp. 396–406, 2013.
- [55] L. Wu, F. Yu, T. N. Do, and J. Wang, "Camera frame misalignment in a teleoperated eye-in-hand robot: Effects and a simple correction method," *IEEE Trans. Hum.-Mach. Syst.*, vol. 53, no. 1, pp. 2–12, Feb. 2023.
- [56] F. L. Markley, Y. Cheng, J. L. Crassidis, and Y. Oshman, "Averaging Quaternion," *J. Guid. Control Dyn.*, vol. 30, pp. 1193–1197, Jul. 2007.
- [57] H. Gao, X. Zhang, C. Ma, and C. Zhou, "Combined active and passive adaptive variable admittance compliant control for space robotic manipulators," in *Proc. IEEE Int. Conf. Rob. Biomimetics*, 2023.
- [58] J. Cho, D. Choi, and J. H. Park, "Sensorless variable admittance control for human-robot interaction of a dual-arm social robot," *IEEE Access*, vol. 11, pp. 69366–69377, 2023.
- [59] L. Roveda, A. A. Shahid, N. Iannacci, and D. Piga, "Sensorless Optimal Interaction Control Exploiting Environment Stiffness Estimation," *IEEE Trans. Contr. Syst. Technol.*, vol. 30, pp. 218–233, Jan. 2022.
- [60] L. Pagliara, E. Ferrentino, A. Chiacchio, and G. Russo, "Safe haptic teleoperations of admittance controlled robots with virtualization of the force feedback," in *Proc. IEEE Int. Conf. Autom. Sci. Eng.*, Aug. 2024, pp. 1574–1579.
- [61] A. Boese, C. Wex, R. Croner, U. B. Liehr, J. J. Wendler, J. Weigt, T. Walles, U. Vorwerk, C. H. Lohmann, M. Friebe, and A. Illanes, "Endoscopic imaging technology today," *Diagn.*, vol. 12, no. 5, May 2022.
- [62] P. Rynio, K. Galant, Ł. Wójcik, B. Grygorcewicz, A. Kazimierzak, A. Falkowski, P. Gutowski, B. Dolegowska, and M. Kawa, "Effects of sterilization methods on different 3d printable materials for templates of physician-modified aortic stent grafts used in vascular surgery—a preliminary study," *Int. J. Mol. Sci.*, vol. 23, no. 7, Mar. 2022.
- [63] E. M. van der Schans, M. A. J. Hiep, E. C. J. Consten, and I. A. M. J. Broeders, "From da vinci si to da vinci xi: realistic times in draping and docking the robot," *J. Robotic. Surg.*, vol. 14, no. 6, pp. 835–839, Dec. 2020.
- [64] R. Steyer and W. Nagel, *Probability and Conditional Expectation: Fundamentals for the Empirical Sciences*. John Wiley & Sons, 2017.
- [65] M. Ruppert, J. Cadosch, J. Guindy, D. Case, and U. Zappa, "In vivo ultrasonic debridement force in bicuspid: A pilot study," *J. Periodontol.*, vol. 73, no. 4, pp. 418–422, 2002.
- [66] D. Stutzer, M. Hofmann, S. Eick, N. Scharp, J. Burger, and T. Niederhauser, "In-vitro measurement of forces during debridement with a piezoelectric ultrasonic periodontal scaler," *Oral Health Prev. Dent.*, vol. 22, 2024. [Online]. Available: <https://pmc.ncbi.nlm.nih.gov/articles/PMC11619864/>

- [67] T. F. Flemmig, G. J. Petersilka, A. Mehl, R. Hickel, and B. Klaiber, "The effect of working parameters on root substance removal using a piezoelectric ultrasonic sealer in vitro," *J. Clin. Periodontol.*, vol. 25, no. 2, pp. 158–163, 1998.
- [68] A. Bangor, P. Kortum, and J. Miller, "Determining what individual SUS scores mean: adding an adjective rating scale," *J. Usability Studies*, vol. 4, no. 3, pp. 114–123, May 2009.
- [69] M. Zhuang, J. Chen, B. Tao, M. Gul, F. Wang, and Y. Wu, "Exploring the learning curve of dental implant placement using a task-autonomous robotic system among young dentists from different specialties—a pilot module study," *Clin. Implant Dent. Relat. Res.*, 2024.
- [70] D. Gagliardi and G. Russo, "On a probabilistic approach to synthesize control policies from example datasets," *Automatica*, vol. 137, p. 110121, 2022.
- [71] E. Garrabe, H. Jesawada, C. Del Vecchio, and G. Russo, "On convex data-driven inverse optimal control for nonlinear, non-stationary and stochastic systems," *Automatica*, vol. 173, p. 112015, 2025.